

Fault Diagnostics in PEMFC Stacks by Evaluation of Local Performance and Cell Impedance Analysis

J. Mitzel^{1,*}, J. Sanchez-Monreal¹, D. Garcia-Sanchez¹, P. Gazdzicki¹, M. Schulze¹, F. Häußler², J. Hunger², G. Schlumberger², E. Janicka³, M. Mielniczek³, L. Gawel³

¹ Institute of Engineering Thermodynamics, German Aerospace Center (DLR), Pfaffenwaldring 38-40, D-70569 Stuttgart, Germany

² Zentrum für Sonnenenergie- und Wasserstoff-Forschung Baden-Württemberg (ZSW), Helmholtzstraße 8, D-89081 Ulm, Germany

³ Department of Electrochemistry, Corrosion and Materials Engineering, Chemical Faculty, Gdansk University of Technology, 11/12 Narutowicza, 80-233 Gdansk, Poland

[*]Corresponding author: Jens.Mitzel@dlr.de

Abstract

Starvation, flooding, and dry-out phenomena occur in polymer electrolyte membrane fuel cells due to heterogeneous local conditions, material inhomogeneity, and uneven flow distribution across the single cell active area and in between the individual cells. The impact of the load level and of the air feed conditions on the performance was identified for individual single cells within a 10-cell stack. Analysis of the current density distribution across the active area at the cell level was correlated with electrochemical impedance spectroscopy to enable *operando* fault diagnostic without any impact of the applied analytical tools on the single cell behavior. Moreover, the combination of both technologies allows in-depth analysis of fault mechanisms in fuel cell single cells with improved sensitivity. Current density distribution and the quantitative assessment of the performance homogeneity demonstrated high sensitivity to small humidity changes and allow the detection of critical events such as dry-out in single cells.

Impedance analysis is more sensitive regarding polarization and diffusion limitations and allows detection of cell flooding. The combination of both techniques is required for reliable identification of air starvation faults.

Keywords: Current Density Distribution, Electrochemical Impedance Spectroscopy (EIS), Fault Diagnostic, Fault Isolation, Operando Analysis, Polymer Electrolyte Membrane Fuel Cell.

1 Introduction

Polymer electrolyte membrane fuel cells (PEMFCs) are highly efficient energy converters and have become more and more important for energy conversion and storage. When fed by green hydrogen, they provide emission free electricity for automotive, stationary, and portable applications [1]. Over the last decades, fuel cell stack materials and fuel cell stack designs have been significantly improved [2,3]. Nevertheless, lifetime of fuel cell stacks under operating conditions in systems are still suffering from severe mechanical, chemical, and physical degradation processes [4,5]. In contrast to other energy converters, the conditions within a PEMFC stack are characterized by gradients and inhomogeneity in various parameters [6].

Due to the low operating temperature and the production of water in fuel cells, the accumulation and removal of liquid water and resulting two phase flow phenomena are the main reasons for inhomogeneous behavior of individual cells in PEMFC stacks [7,8]. On the other hand, an insufficient level of humidification makes the ionic conductivity of the membrane to decrease, resulting also in a reduction of performance [9,10].

It was shown that water management in the cells can be directly linked to degradation processes and non-optimal conditions can shorten PEMFC lifetime significantly [9,11,12]. As a consequence, fault diagnostic in PEMFC stacks (e.g. regarding dry-out and cell flooding) is

highly important to (i) assure reliable fuel cell operation and (ii) to maximize the stack lifetime in a system. These systems are complex and the stack performance is influenced by coupling effects of fluid dynamics, uneven heat distribution, occurring electrochemical reaction, and phase changes of water [13]. Additionally, the different behaviors of the single cells can result in severe stack damage [14]. Specifically, a critical failure in a single cell usually means a critical failure of the entire stack. Due to this complexity, faulty operation of the PEMFC stack has a major impact on reliability and maintenance costs of the entire system.

Thus, diagnostic is a key technology to assure long lifetime and highly efficient operation of the fuel cell stack. Due to reliable isolation of faults, the control unit of a fuel cell system can initiate appropriate counteractions and modify the operating parameters of the balance of plant components to assure stack operation in non-critical conditions.

Several review articles consider PEMFC stack diagnostic and monitoring [15,16]. The focus of these reviews is on data analysis using different model-based and non-model-based approaches. However, these models are based on data from cell voltage measurements (CVM). Several electrochemical methods have been applied to analyze processes in PEMFC stacks in more detail [17]. Such techniques can improve the understanding of occurring degradation phenomena and of fault mechanisms. Some of these methods do not provide *operando* information. However, electrochemical impedance spectroscopy (EIS) and total harmonic distortion analysis (THDA) have proven to provide insides into operating PEMFC stacks. Thereby, EIS has been demonstrated to be an important non-invasive *in situ* technique to investigate the different processes occurring within individual cells of a PEMFC stack and to identify cells operating under critical conditions [18,19]. This technique only provides information about the behavior of a single cell without local resolution over the active area. THDA is a technique that minimizing the equipment cost and analysis time and enabling easy

implementation into PEMFC systems. The technique is focused on the detection of faults in the entire stack and not on the identification of faulty single cells within a stack [20].

To obtain information on local effects across the active area, measurements of the current density and temperature distribution are required. Segmented bipolar plates based on printed circuit boards (PCBs) are a patented technology by DLR [21,22]. These devices measure the voltage drop along a defined resistor shunt in each segment while the current is passing the segmented bipolar plate. This measurement device acts as regular bipolar plate and has negligible impact on the system. PCB technology enables the evaluation of the local current density distribution over the active area of a single cell and allows direct observation of local gradients and temporal fluctuations of the electrochemical activity. Depending on time scale and pattern, local condensation of liquid water, oscillating reaction fronts, irreversible local degradation, or other undesired conditions can be identified [9,23]. Local current density measurements have been used by different research groups to investigate the impact of critical conditions and faults in PEMFCs. These investigations were mainly realized in single cells and analysis of dehydration and dry-out [23,24], reactant starvation [25,26,27], water management [9,28], and flooding processes [24,29,30] were included. The application of this technique to multi cell stacks is rare [31,32,33,34,35,36]. None of the available investigations has combined the analysis of the local current density distribution in several single cells of the stack with impedance analysis of these single cells to analyze the possible fault mechanisms in an operating PEMFC stack.

Furthermore, the different technologies have limitations and advantages in terms of sensitivity, local resolution and obtained information. Fault detection and isolation as well as the identification of all potential fault mechanisms cannot be realized using only one of these methods. In the presented work, the combination of two technologies allows in-depth analysis of fault mechanisms. Determination of the current density distribution across the active area

was combined with EIS on the single cell level. The objective of this work was the analysis of the faulty conditions and of the degradation phenomena in fuel cell stacks operating under system relevant conditions. This study was focused on the behavior of a 10-cell PEMFC stack being subject to different load levels and to critical operating conditions at the cathode side. This combined study allows reliable detection of different fault modes and identifies reasons for increased local degradation effects in PEMFC stacks. Consequently, this in-depth analysis of fault mechanisms can enable fuel cell diagnostic in single cells with higher sensitivity towards occurring faults during system operation.

2 Experimental

2.1 Fuel Cell Stack

The presented tests were carried out using a liquid-cooled PEMFC stack manufactured by ZSW (Zentrum für Sonnenenergie- und Wasserstoff-Forschung Baden-Württemberg). This stationary stack of 480 W nominal electrical power output was equipped with ten cells of an active electrode area of 96 cm² using graphitic composite bipolar plates. Three PCBs for measuring the current density distribution were included in the stack. The first PCB was integrated in the first cell close to the anodic current collector (referred to cell with index 01), the second PCB in the middle of the stack (cell 05) and the third PCB in cell 10 close to the cathodic current collector and the media supply ports (Figure 1 (A)). Multiple serpentine flow fields were used in the bipolar plates on the anode and on the cathode side. The resulting media flow configurations in each cell and the applied segmentations are shown in Figure 1 (B).

2.2 Test Station

Fuel cell tests were carried out using an DLR in-house manufactured 1 kW test station using hydrogen (grade 5.0) and compressed ambient air (particle-filtered, dried and oil-free). The test bench is equipped with programmable logic controllers (PLCs) and commercial electronic loads. It allows automatic control of the operating cell conditions, such as humidity of the reactants, cell temperature, gas flow rates and stack pressure. The relative humidity (RH) of the inlet gases is controlled by direct evaporators and high precision liquid mass flow controllers by Bronkhorst HIGH-TECH BV. The stack temperature is adjusted by an Integral XT 8 HW thermostat (Lauda Dr. R. Wobser GmbH & Co. KG) using deionized water for coolant. All stack reactant supply pipes are electrically heated and thermally insulated to avoid water condensation in the feed streams. The reactant flow is adjusted by gas mass flow controllers (red-y smart series by Vögtlin Instruments AG) and the reactant pressure by pressure controllers (EL-PRESS by Bronkhorst). A ZS Electronic Load (Höcherl & Hackl GmbH) is used for stack current control. All test operation parameters are controlled according to the guidelines for reliable PEMFC stack testing defined in the European Stack-Test project [6].

2.3 Impedance Setup

EIS allows the differentiation between nominal operation and operation under critical conditions, such as flooding, dry-out or reactant starvation [37,38]. Furthermore, EIS devices using multiple, parallel channels can be used to identify inhomogeneous operation of individual cells. A combined device for parallel cell measurements was used for EIS data acquisition and analysis (ZAHNER-elektrik GmbH & Co. KG). All measurements were realized in galvanostatic EIS mode. An electronic load EL1000 was used to apply the sinoidal current signal to the entire stack. An IM6 potentiostat equipped with four PAD4 modules was used to measure the voltage response of the stack and of the 10 single cells, respectively. Spectra were

obtained from 10 kHz to 0.1 Hz. Above 66 Hz ten logarithmically spaced frequencies were measured for each decade using 20 measure periods each. Below 66 Hz five logarithmically spaced frequencies were measured for each decade using 4 measure periods each, resulting in data acquisition time of about 5 minutes. The AC amplitude was adapted to the DC load level to assure linear EIS response with good signal-to-noise ratio (Table 1). Data acquisition and analysis was carried out using the Thales XT 5.2.0 software.

The simplified equivalent circuit presented in Figure 2 (A) was used to fit the EIS data in this work. This equivalent circuit consists of a serial connection of the following elements: (i) an inductivity L for the cables in the setup, (ii) an ohmic resistance R_{el} mainly dominated by the electrolyte resistance (membrane), (iii) an RC element (parallel element of an ohmic resistance R_{pol} and a capacitor C_{pol}) for the polarization reaction, and (iv) an RC element for mass transport limitation dominated by diffusion processes (R_{diff} and C_{diff}).

2.4 Current Density Distribution

The used PCBs for the measurement of the current density and temperature distribution were specially design for parallel use in the examined stack and manufactured by “Helmbold - Messtechnik für Brennstoffzellen”. 81 segments for current density measurement and 8 sensors for temperature measurement were included in each PCB. The data acquisition was realized using a 34980A Multifunction Switch/Measure Unit (Keysight Technologies) equipped with six 34922A 70-channel multiplexer modules. Resulting data acquisition time was about 4 seconds. Data processing and visualization was carried out using a DLR in-house programmed LabView application.

3 Results and Discussion

3.1 Impact of Electrical Load Level

The current-voltage characteristic of the investigated stack is shown in Figure 2 (B). The stack was operating under nominal conditions as defined by the stack manufacturer and as described in the following. The stack temperature was controlled to 80 °C according to the coolant temperature at the stack inlet and the feed gases were heated to 85 °C to avoid water condensation. Hydrogen and air stoichiometry of 1.5 and 2.0 were applied, respectively. The reactant pressure was controlled to 150 kPa_{abs} at the stack outlet and the relative humidity of the reactants was adjusted to 30% at the stack inlet. To avoid starvation issues in case of current densities below 0.2 A cm⁻², the minimum flow rate was fixed at the value corresponding to the mentioned stoichiometry at 0.2 A cm⁻². The analyzed current voltage curve was measured in the direction of descending electrical load from 1.0 A cm⁻² to open circuit voltage.

It is obvious that the cell performances do not vary under these nominal conditions over the entire load range applied. The average cell voltage at 1.0 A cm⁻² is 632 mV with a maximum deviation of 15 mV. Consequently, it is not possible to obtain detailed information about individual cell behavior during current density changes based only on the obtained linear polarization results. The non-linear behavior of the current voltage characteristic below 0.2 A cm⁻² due to dominating polarization effects (activation over-potentials) is clearly visible while mass-transport limitations are only slightly detectable at current densities higher than 0.8 A cm⁻². The high homogeneity of the single cell performance reveals that the integrated PCBs have no impact on cell operation.

For more detailed analysis of the stack behavior at the load levels indicated in Figure 2 (B), the current density distribution and the impedance response in the individual cells were evaluated. For this study, three operating points A-C in the activation control regime (0.02, 0.05, and 0.2 A cm⁻²), two operating points D-E in the mixed control regime (0.4 and 0.7 A cm⁻²), and one

operating point F in the mass transport control regime (1.0 A cm^{-2}) were analyzed. The results from the current density measurement of the three PCBs at these operating points are depicted in Figure 3. For comparative visualization of the current density distribution, all results in this work are presented in relative values and scaled to $\pm 20\%$ deviation from the set value of each operating point. E.g. for the operating point at 1.0 A cm^{-2} , current density is visualized from 0.8 (dark blue) to 1.2 A cm^{-2} (dark red) in Figure 3 (F).

Based on the visualization of the current density distribution, there is only a minor impact on the homogeneity of the current density distribution in the activation control regime (Figure 3 (A)-(C)). The maximum of the current density is located in the center of the active area. Due to the over-stoichiometric operation in this regime, the mass transport limitation impact by lowering the oxygen concentration along the cathode flow field cannot be detected. With increasing load level in the mixed control regime (Figure 3 (D)-(E)), this limitation increases and is particularly strong in the transport control regime (Figure 3 (F)). As a consequence, the maximum of the current density shifts from the center of the active area towards the air inlet (bottom left corner). The current density close to the air outlet (top right corner) is significantly lower due to reduced oxygen concentration in the flow field. It is also obvious that the stack performance homogeneity is not only a function of the load level, but also of the cell position within the stack. The highest inhomogeneity is visible in cell 10 close to the media inlets (hydrogen, air, and coolant), while cell 01 at the opposite side of the stack is operating homogeneously and the impact of the load level is lower in this cell.

For quantitative assessment of the performance homogeneity, the current density distribution results from Figure 3 are converted to Box-Whisker plots shown in Figure 4 (A). Each box demonstrates the area in which the middle 50% of the related data set is located and the median is included as a line in the box. Consequently, the size of the box is a measure of the homogeneity of the data, which is determined by the difference between the upper and lower

quartile. The included whiskers reach up to the largest and smallest value from the data set and represent the spread of the extreme values. It is obvious that the impact of the electrical load level on the quantitative results of the current density distribution is negligible, but the significant higher homogeneity of cell 01 is clearly visible. The current density values of cell 01 inside the box are in the range of about $\pm 5\%$ from the set value, while these values differ about $\pm 12\%$ for cell 05 and cell 10. For cell 01, the extreme values (whiskers) are within a range of $\pm 15\%$. In contrast, the maximum values for cell 05 and cell 10 are about 24% higher than the set value and the minimum values are about 36% lower.

Figure 4 (B) shows the single cell voltages of the three analyzed cells at the different examined load levels. There is no difference in the cell performances detectable in the activation control regime up to 0.2 A cm^{-2} . For higher current densities, the performance of the most uniform cell 01 is slightly higher (637 mV at 1 A cm^{-2}) compared to cells 05 and cell 10 (618 mV and 626 mV).

The EIS response of all single cells at the examined load levels are shown in Figure 5. The shape of the obtained spectra is strongly depending on the applied load level. In the activation control regime (Figure 5 (A)-(C)) the polarization resistance is dominant. This is most pronounced at 0.02 A cm^{-2} (Figure 5 (A)) where only one semi-arc is visible. The diameter of this semi-arc at high frequencies decreases with increasing current density (Figure 5 from (A) to (E)). Consequently, the polarization resistance R_{pol} decreased with increasing load from 1.92 to $0.15 \text{ } \Omega \text{ cm}^2$ as can be seen from EIS data analysis via fitting which is provided in Figure 5 (G). Simultaneously, a second semi-arc at lower frequencies appears and increases with increasing current density. This semi-arc is caused by mass transport limitations. The resulting diffusion resistance R_{diff} , also shown in Figure 5 (G), is increasing from $0.07 \text{ } \Omega \text{ cm}^2$ at 0.2 A cm^{-2} to $0.48 \text{ } \Omega \text{ cm}^2$ at 1.0 A cm^{-2} . In the transport control regime at 1.0 A cm^{-2} (Figure 5 (F)), this mass transport limitation is dominant. Furthermore, R_{diff} increases also for current densities

below 0.2 A cm^{-2} to $0.24 \Omega \text{ cm}^2$ at 0.05 A cm^{-2} and to $0.31 \Omega \text{ cm}^2$ at 0.02 A cm^{-2} . This increase can be explained by the over-stoichiometric operation in this region and the resulting dry-out of the ionomer in the catalyst layer. It is known that the oxygen permeability through ionomer films decreases under dry conditions [39], which limits the oxygen access to the catalyst. The analysis of the electrolyte resistance R_{el} is presented in Figure 5 (G). R_{el} decreases with increasing electrical load from 0.23 to $0.07 \Omega \text{ cm}^2$ due to increasing water production and membrane humidification. Below 0.2 A cm^{-2} R_{el} is significant higher due to membrane dry-out caused by the over-stoichiometric operation in this region.

It is obvious that the impedance spectra of all single cells are similar and differences are negligible. No significant variations in R_{el} , in the polarization resistance, or in the transport resistance can be detected for a certain single cell under the applied nominal conditions. This indicated that applied nominal operating conditions enable homogeneous, non-critical operation of the examined stack. The inhomogeneous cell behavior as obvious in the current density distribution (Figure 3 and Figure 4) is not detectable by EIS. This shows that the current density distribution is more sensitive to small changes in the individual cell operation, even if these have minor impact on the cell voltage and the impedance response averaged over the entire active area of the cells. Thereby, the sensitivity of the current density distribution is not only accessible by the quantitative changes in the homogeneity, but also by the location of the current density maximum in relation to the air inlet. Furthermore, it can be concluded that non-linear responses are not an issue for the applied single cell EIS analysis under these conditions.

3.2 Impact of Cathode Dry-out and Flooding

To validate the applied methodology for cathodic faults, the stack was operated under critical conditions. First, the impact of cathode dry-out and flooding was studied. These tests were realized at a current density of 0.5 A cm^{-2} . Operating parameters were the same as specified in

section 3.1, but the cathode humidity level was adapted. Therefore, the relative humidity of the applied air feed (RH_{air}) was varied between 0% and 100%.

The visualization of the current density distribution is shown in Figure 6 using relative values. Single cell dry-out can be detected by current density distribution when non-humidified air is fed to the stack (Figure 6 (A)). A large area of low current density is obtained close to the air inlet (bottom left corner). Also at low relative air humidity of 20% (Figure 6 (B)), the current density is decreased close to the air inlet. This effect may be a result of membrane and catalyst layer dry-out and is in line with further studies on the impact of reactant inlet humidity [10]. Due to water production, the humidity of the air in the flow field increases along the flow channels and the current density maximum is located slightly shifted to the upper part of the cell. This detected dry-out effect is most visible for cell 10 close to the media inlet and less pronounced in cell 01. The measurements demonstrate that the impact of the air humidity is highest in the range of 0% to 50% (Figure 6 (A) to (C)). The maximum current density shifts towards the air inlet if the air inlet humidity is increased. The most homogeneous behavior is reached at 20% relative humidity, i.e. at conditions close to the nominal conditions (see Figure 3). The current density distribution changes in the range of 75% to 100% are not significant, but feed air humidification of 50% and more clearly results in a higher inhomogeneity of the current density compared to the nominal conditions. However, the difference between the individual cells in this region is less pronounced compared to the dry-out effect.

The quantitative assessment of the impact of the air inlet humidity on the performance homogeneity is given in Figure 7 (A). As already visible in Figure 6, cell 01 is almost not affected by the humidity variation. The homogeneity only slightly increases for the box values from $\pm 6\%$ to $\pm 5\%$ and for the extreme values from $\pm 20\%$ to $\pm 15\%$ with increasing air inlet humidity. In contrast, the homogeneity of cell 05 and cell 10 clearly increases with increasing air inlet humidity. Without humidification, the current density distribution is highly

inhomogeneous. The values inside the box differ about $\pm 25\%$. The maximum values are about 40% higher and the minimum values are up to 75% lower compared to the set value of 0.5 A cm^{-2} . Especially, the low performance close to the air inlet is remarkable. With increasing air inlet humidity the performance homogeneity in these cells improves and fully humidified air results in a difference of the values inside the box of about $\pm 6\%$. The maximum deviation of the values is about 20% and the minimum deviation is about 30%.

The comparison to the single cell voltages in Figure 7 (B) shows that a high cell voltage and thus a high cell performance are not always connected to high homogeneity in the cell behavior. Non-humidified conditions result in low single cell voltage and low homogeneity. But the highest single cell voltages are achieved using 20% air inlet humidity, while highest homogeneity is achieved at higher humidity of at least 75%.

The single cell EIS responses during this study are shown in Figure 8. Apparently, the cell spectra are more distinguishable from each other compared to operation under nominal conditions in Figure 5 where all cell behaved similarly. The EIS analysis shows that the differences in R_{el} between the single cells is not affected by the humidity level, but R_{el} decreases significantly when the humidification is increased. As already visible in the current density measurements, the impact of the relative humidity on the cell performance is highest between 0% and 50% (Figure 8 (A) to (C)). In this region R_{el} decreases from $0.12 \text{ } \Omega \text{ cm}^2$ and remains almost constant for high humidification (Figure 8 (G)). Consequently, the relevant diagnostic parameters for the assessment of cell dry-out phenomena are the R_{el} increase by EIS and the decrease of the current density at the air inlet by PCB. It was shown that the current density measurements are significantly more sensitive regarding the dry-out of individual cells for this application.

The analysis of R_{pol} ($0.27 \text{ } \Omega \text{ cm}^2$) and R_{diff} ($0.30 \text{ } \Omega \text{ cm}^2$) shows that both values are also increased if the air feed is not humidified. Again, this seems to be caused by the electrolyte dry-

out in the catalyst layer and the significant decrease of oxygen permeability through ionomer films [39], which limits the oxygen access to the catalyst. As soon as the fed air is humidified (Figure 8 (B) to (F)) R_{pol} increases from 0.16 to 0.30 $\Omega \text{ cm}^2$ and R_{diff} increases from 0.25 to 0.38 $\Omega \text{ cm}^2$ (Figure 8 (G)) with increasing humidification. This indicates that formation of liquid water in the catalyst layer and in the flow field can also limit the oxygen availability at the catalyst surface. It can be observed that this increase in R_{pol} and R_{diff} is different in the individual cells, which is clearly visible at 50% relative humidity in Figure 8 (C) and in the high standard deviation in Figure 8 (G). While the increase of these resistances in cells 03 to 09 is comparable, cells 01, 02, and 10 shows significant higher changes. R_{pol} for cells 01, 02, and 10 with $(0.33 \pm 0.09) \Omega \text{ cm}^2$ is about 2.8-times higher compared to R_{pol} for cells 03 to 09 with $(0.12 \pm 0.03) \Omega \text{ cm}^2$. R_{diff} for cells 01, 02, and 10 with $(0.40 \pm 0.07) \Omega \text{ cm}^2$ is about 1.4-times higher compared to R_{diff} for cells 03 to 09 with $(0.29 \pm 0.03) \Omega \text{ cm}^2$. There seems to be a transitional behavior regarding flooding phenomena at 50% relative humidity with direct impact on the cell performance. Cells 01, 02, and 10 are affected by flooding while the other cells are not. Above 50% relative humidity all single cells seems to be affected. For this flooding phenomenon, EIS has shown higher sensitivity compared to current density measurements, where the difference in the individual cell behavior was not detectable.

3.3 Impact of Air Starvation

To study the impact of air starvation, the stoichiometry of the air supply (λ_{air}) was stepwise lowered starting from the nominal value 2.0 down to 1.5 using an air inlet relative humidity of 100%. All other parameters remain on the nominal values as specified in section 3.1.

The current density measurement results of this study at a load level of 0.5 A cm^{-2} are presented in Figure 9. While the current density distribution at an air stoichiometry of 2.0 is quite

homogeneous, the behavior of the single cells under decreased air flow changes significantly and more pronounced in the cells close to the media inlet (high index single cells). Due to the decreased air flow, the depletion of the oxygen in the air is higher and the maximum current density shifts towards the air inlet (bottom left corner). The depleted zone with low current density is obvious at the air outlet (top right corner), especially in cell 10 at λ_{air} of 1.5. The impact of low λ_{air} on the current density distribution of the individual cells is diverse. While the homogeneity of cell 10 near to the media inlets is low, cell 01 on the opposite side of the stack operates quite homogenous. Consequently, air starvation issues can be detected in cell 10 at λ_{air} values below 1.8, in cell 05 below 1.7 and not even at 1.5 in cell 01.

The realized current density distribution measurements are analyzed quantitatively as shown in Figure 10 (A). This assessment confirms the visual result that lowering the air flow has the highest impact on cell 10. At an air stoichiometry of 2.0, cell 10 shows comparable homogeneity to cell 01 and cell 05 with a range of the values inside the box of about $\pm 6\%$, a maximum deviation of about 20% and the minimum deviation of 20-30%. These values only slightly increase for cell 01 and cell 05 when the air stoichiometry is lowered. In contrast, the changes for cell 10 are significant. For an air stoichiometry of 1.5, the range of the values inside the box increases to about $\pm 12\%$ and the maximum and minimum deviation to about 50%.

The impact of the air stoichiometry on the single cell voltages of the three analyzed cells is shown in Figure 10 (B). In general, the single cell voltages decrease with decreasing air stoichiometry. But there is no clear link between the homogeneity of the cell behavior and the single cell voltages. Even highly notable differences in the current density distribution and clear air starvation issues result in only slight changes of the single cell voltages. At λ_{air} of 2.0, the distribution of the current density of all three cells is comparable and the single cell voltages differ about 8 mV. The significant difference in current density distribution at λ_{air} of 1.5 and the starvation issue in cell 10 result in a single cell voltage difference of about 20 mV, an

increase of only 12 mV. Consequently, the observation of the single cell voltages is not sufficient to detect air starvation in a single cell.

The results of the EIS analysis under air starvation conditions are summarized in Figure 11. The relative humidity of the fed air was constant at 100% in this study. Consequently, the impact on R_{el} is minor. Neither the absolute value of R_{el} with $0.06 \Omega \text{ cm}^2$ nor the deviation of R_{el} between the cells changes significantly when λ_{air} is lowered. Also the impact on R_{pol} is minor. The average value of R_{pol} decreases with decreasing λ_{air} from 0.38 to $0.34 \Omega \text{ cm}^2$ by about 11%. Significant changes in the deviation of R_{pol} between the individual cells could not be detected.

The main impact of lowering λ_{air} from 2.0 to 1.5 (Figure 11 (A) to (F)) is detectable by changes in R_{diff} (Figure 11 (G)). The average value of R_{diff} increases by about 2.7-times from 0.29 to $0.79 \Omega \text{ cm}^2$ and the standard deviation between the individual cells increases by about 5.8-times from 0.06 to $0.35 \Omega \text{ cm}^2$. These increases are detectable over the entire range of λ_{air} . Lowering the air inlet flow has also an impact on the stability of the EIS measurements. At λ_{air} values of 1.6 (Figure 11 (E)) and 1.5 (Figure 11 (F)), the EIS response at low frequencies becomes instable due to temporal instability in the single cell voltages. These instabilities are caused by the accumulation of liquid water droplets in the cathodic flow field and impede the reliable measurement and interpretation of EIS below about 2 Hz. The mentioned voltage instabilities were particularly strong for cell 10, showing the highest inhomogeneity in the current density distribution (Figure 9 and Figure 10). Nevertheless, also cell 01 was affected, which showed the highest homogeneity in the PCB measurements. This aspect shows that mass-transport issues can occur even if the current density distribution is homogeneous.

Consequently, none of both applied techniques enables full information about starvation faults. Yet, the combination of both enables high sensitive detection of such fault. Oxygen depletion and starvation can be detected by increased R_{diff} using EIS to avoid low efficient cell operation.

Inhomogeneous cell operation can be detected by current density distribution using PCBs to avoid stack operation under conditions with high stress on the components and with negative impact on the stack lifetime.

4 Conclusions

The presented work has demonstrated that current density and impedance measurements can be applied to PEMFC stacks for improved diagnostic without impacting single cell operation and performance.

It can be concluded that the combination of both examined technologies, EIS and current density measurements, allows in-depth analysis of fault mechanisms and can enable the diagnostic of fuel cell single cells with improved sensitivity. Thereby, PCBs and the quantitative assessment of the performance homogeneity are more sensitive to small changes in the humidity levels and to the detection of dry-out phenomena of individual cells. On the other hand, EIS is more sensitive regarding flooding phenomena due to the detection of polarization and diffusion limitations. The combination of both techniques is required for reliable identification of air starvation faults. Oxygen depletion and starvation can be detected by increased R_{diff} using EIS and inhomogeneous cell operation can be detected by current density distribution using PCBs.

Thus, the combination of both techniques improves the identification and isolation of cathodic flooding, air starvation and cell dry-out. Using these findings, the diagnostic for PEMFC stacks can be improved to avoid critical conditions and to increase lifetime and efficiency during system operation.

Acknowledgements

The presented work is realized in the COALA project (control algorithm and controller for increasing the efficiency of hybrid PEMFC systems in different applications) in the framework of the Polish-German Sustainability Research Call (STAIR II). The funding for this research was received from the National Center for Research and Development (NCBR, Poland) and the Federal Ministry of Education and Research (BMBF, Germany) with the Grant No.: STAIR/6/2016 and 01LX1601, respectively.

The authors gratefully acknowledge Siegfried Graf, Stefan Anderle, and Olivier Garrot for the installation of the used test equipment and the development of the LabView applications for test bench control as well as data acquisition and visualization.

List of Symbols

L : inductivity for the cables in the setup / H

R_{el} : electrolyte resistance / $\Omega \text{ cm}^2$

R_{pol} : polarization resistance / $\Omega \text{ cm}^2$

C_{pol} : polarization capacitor / F

R_{diff} : diffusion resistance / $\Omega \text{ cm}^2$

C_{diff} : diffusion capacitor / F

RH_{air} : relative humidity of the applied feed air / %

λ_{air} : stoichiometry of the air supply / -

CVM: cell voltage measurement

EIS: electrochemical impedance spectroscopy

PCB: printed circuit board

PEMFC: polymer electrolyte membrane fuel cell

THDA: total harmonic distortion analysis

References

- [1] I. Staffell, D. Scamman, A. Velazquez Abad, P. Balcombe, P.E. Dodds, P. Ekins, N. Shah, K.R. Ward, *Energy Environ. Sci.* **2019**, 12, 463.
- [2] A. Kraytsberg, Y. Ein-Eli, *Energy Fuels* **2014**, 28, 7303.
- [3] N. Konno, S. Mizuno, H. Nakaji, Y. Ishikawa, *SAE Int. J. Alt. Power* **2015**, 4, 123.
- [4] R. Borup, J. Meyers, B. Pivovar, Y.S. Kim, R. Mukundan, N. Garland, D. Myers, M. Wilson, F. Garzon, D. Wood, P. Zelenay, K. More, K. Stroh, T. Zawodzinski, J. Boncella, J.E. McGrath, M. Inaba, K. Miyatake, M. Hori, K. Ota, Z. Ogumi, S. Miyata, A. Nishikata, Z. Siroma, Y. Uchimoto, K. Yasuda, K.-I. Kimijima, N. Iwashita, *Chem. Rev.* **2007**, 107, 3904.
- [5] F.A. De Bruijn, V.A.T. Dam, G.J.M. Janssen, *Fuel Cells* **2008**, 8, 3.
- [6] J. Mitzel, E. Gülzow, A. Kabza, J. Hunger, S.S. Araya, P. Piela, I. Alecha, G. Tsotridis, *Int. J. Hydrogen Energy* **2016**, 41, 21415.
- [7] K. Jiao, B. Zhou, P. Quan, *J. Power Sources* **2006**, 154, 124.
- [8] A. Bozorgnezhad, M. Shams, H. Kanani, M. Hasheminasab, G. Ahmadi, *Int. J. Hydrogen Energy* **2016**, 41, 19164.
- [9] D. Garcia Sanchez, T. Ruij, I. Biswas, M. Schulze, S. Helmly, K. A. Friedrich, *J. Power Sources* **2017**, 352, 42.
- [10] D. Garcia Sanchez, T. Ruij, K.A. Friedrich, J. Sanchez-Monreal, *J. Electrochem. Soc.* **2016**, 163, F150.
- [11] M. Schulze, K.A. Friedrich, *ECS Trans.* **2008**, 12, 101.
- [12] N. Yousfi-Steiner, P. Moçotéguy, D. Candusso, D. Hissel, A. Hernandez, A. Aslanides, *J. Power Sources* **2008**, 183, 260.
- [13] T.-F. Cao, H. Lin, L. Chen, Y.-L. He, W.-Q. Tao, *Applied Energy* **2013**, 112, 1115.

- [14] M. Hinaje, D. Nguyen, S. Raël, B. Davat, C. Bonnet, F. Lapicque, *Int. J. Hydrogen Energy* **2009**, 34, 6364.
- [15] Z. Zheng, R. Petrone, M.C. Péra, D. Hissel, M. Becherif, C. Pianese, N. Yousfi Steiner, M. Sorrentino, *Int. J. Hydrogen Energy* **2013**, 38, 8914.
- [16] R.-H. Lin, X.-N. Xi, P.-N. Wang, B.-D. Wu, S.-M. Tian, *Int. J. Hydrogen Energy* **2019**, 44, 5488.
- [17] J. Wu, X.Z. Yuan, H. Wang, M. Blanco, J.J. Martin, J. Zhang, *Int. J. Hydrogen Energy* **2008**, 33, 1735.
- [18] S. Strahl, N. Gasamans, J. Llorca, A. Husar, *Int. J. Hydrogen Energy* **2014**, 39, 5378.
- [19] S. Rodat, S. Sailler, F. Druart, P.-X. Thivel, Y. Bultel, P. Ozil, *Journal of Applied Electrochemistry* **2010**, 40, 911.
- [20] E. Ramschak, V. Peinecke, P. Prenninger, T. Schaffer, V. Hacker, *J. Power Sources* **2006**, 157, 837.
- [21] S. Schönbauer, H. Sander, DE Patent, DE 10316117 B3, **2004**.
- [22] T. Kaz, H. Sander, S. Schönbauer, EP Patent, EP 1618395 A1, **2006**.
- [23] D. Garcia Sanchez, P. L. Garcia Ybarra, *Int. J. Hydrogen Energy* **2012**, 37, 7279.
- [24] Z. Liu, Z. Mao, B. Wu, L. Wang, V. M. Schmidt, *J. Power Sources* **2005**, 141, 205
- [25] Y. Yu, X. Z. Yuan, H. Li, E. Gu, H. Wang, G. Wang, M. Pan, *Int. J. Hydrogen Energy* **2012**, 37, 15288.
- [26] M. Dou, M. Hou, D. Liang, Q. Shen, H. Zhang, W. Lu, *J. Power Sources* **2011**, 196, 2759.
- [27] Z. Liu, L. Yang, Z. Mao, W. Zhuge, Y. Zhang, L. Wang, *J. Power Sources* **2006**, 157, 166.

- [28] J. Stumper, S. A. Campbell, D. P. Wilkinson, M. C. Johnson, M. Davis, *Electrochim. Acta* **1998**, 43, 3773.
- [29] A. Hakenjos, H. Muentert, U. Wittstadt, C. Hebling, *J. Power Sources* **2004**, 131, 213.
- [30] T. V. Reshetenko, G. Bender, K. Bethune, R. Rocheleau, *Electrochim. Acta* **2011**, 56, 8700.
- [31] L. C. Perez, L. Brandao, J. M. Sousa, A. Mendes, *Renew Sust Energ Rev* **2011**, 15, 169.
- [32] Q. Meyer, K. Ronaszegi, J. B. Robinson, M. Noorkami, O. Curnick, S. Ashton, A. Danelyan, T. Reisch, P. Adcock, R. Kraume, P. R. Shearing, D. J. L. Brett, *J. Power Sources* **2015**, 297, 315.
- [33] M. Schulze, E. Gülzow, S. Schonbauer, T. Knöri, R. Reissner, *J. Power Sources* **2007**, 173, 19.
- [34] P. C. Ghosh, T. Wuster, H. Dohle, N. Kimiaie, J. Mergel, D. Stolten, *J. Power Sources* **2006**, 154, 184.
- [35] M. Santis, S. A. Freunberger, M. Papra, A. Wokaun, F. N. Büchi, *J. Power Sources* **2006**, 161, 1076.
- [36] F. N. Büchi, A. B. Geiger, R. P. Neto, *J. Power Sources* **2005**, 145, 62.
- [37] K. Darowicki, E. Janicka, M. Mielniczek, A. Zielinski, L. Gawel, J. Mitzel, J. Hunger, *Electrochim. Acta* **2018**, 292, 383.
- [38] K. Darowicki, E. Janicka, M. Mielniczek, A. Zielinski, L. Gawel, J. Mitzel, J. Hunger, *Applied Energy* **2019**, 251, 13396.
- [39] K. Broka, P. Ekdunge, *Journal of Applied Electrochemistry* **1997**, 27, 117.

Figures

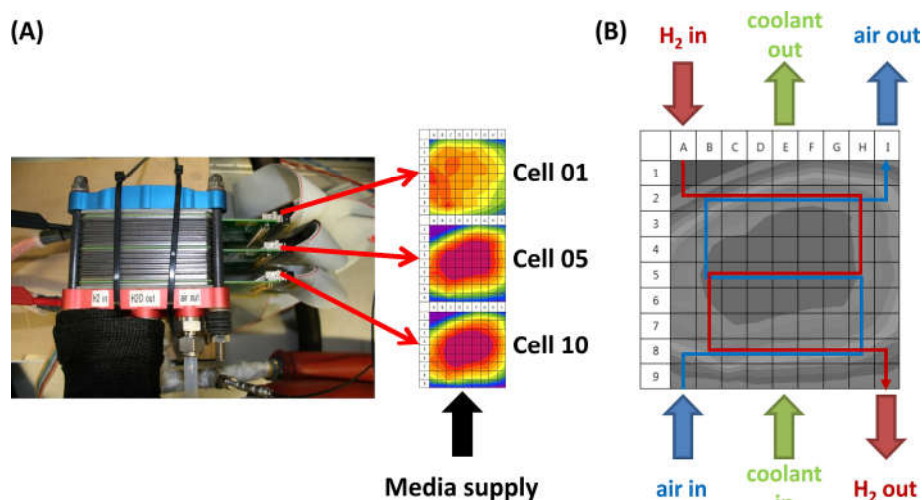


Figure 1: Experimental setup of the examined stack: (A) PCBs integrated in cell 01 at anodic current collector, in cell 05, and in cell 10 at cathodic current collector and media supply ports (cell index defines single cell position in the stack starting from anodic current collector); (B) Segmentation and media flow configuration in each single cell.

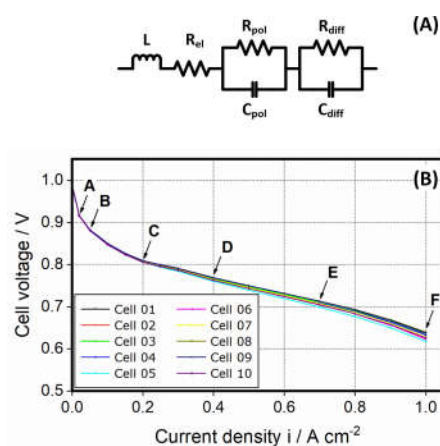


Figure 2: Applied equivalent circuit for EIS analysis (A) and current voltage characteristic of examined stack including operation points (A-F) for PCB and EIS analysis shown in Figure 3 and Figure 4 (B).

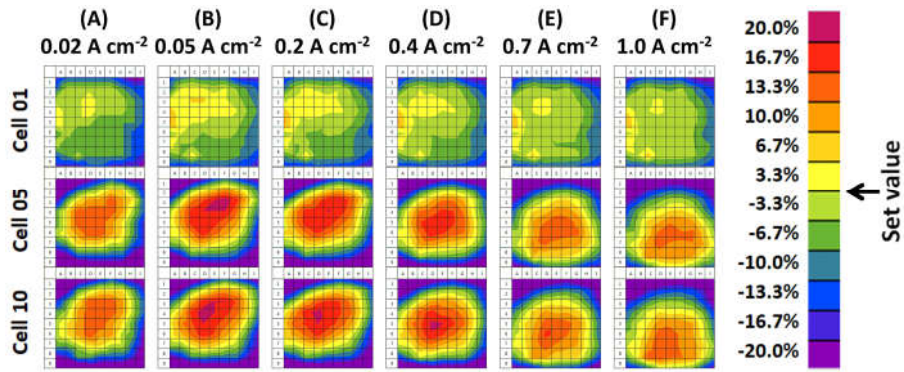


Figure 3: Current density distribution at different operating points of the current voltage characteristic shown in Figure 2. Operation in the activation control regime was analyzed at 0.02 (A), 0.05 (B), and 0.2 A cm⁻² (C). Operation in the mixed control regime was analyzed at 0.4 (D) and 0.7 A cm⁻² (E). Operation in the transport control regime was analyzed at 1.0 A cm⁻² (F). Results are presented in relative values and scaled to $\pm 20\%$ deviation from the set value of each operating point. Cell and media flow configuration is given in Figure 1.

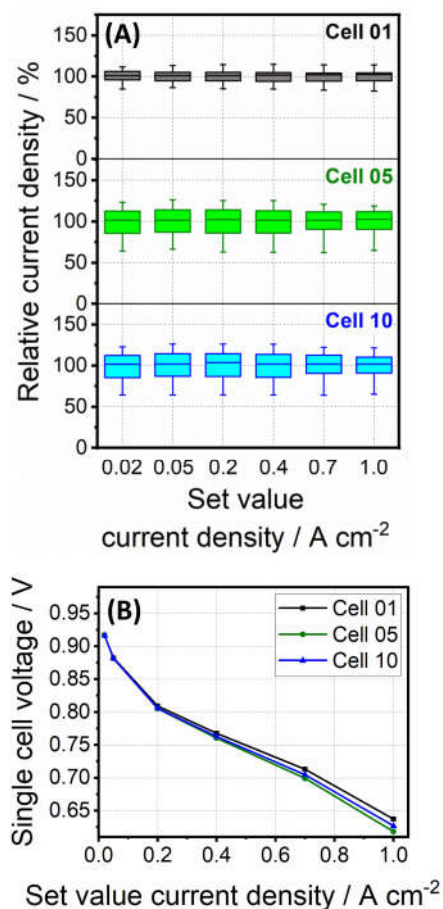


Figure 4: Box-Whisker plots (A) of the current density distribution measurements shown in Figure 3. Each box shows the area in which the middle 50% of the related data set is located. The median is included as a line in the box. The whiskers reach up to the largest and smallest value from the data. Single cell voltages of the three analyzed cells at different operating points are shown in panel (B).

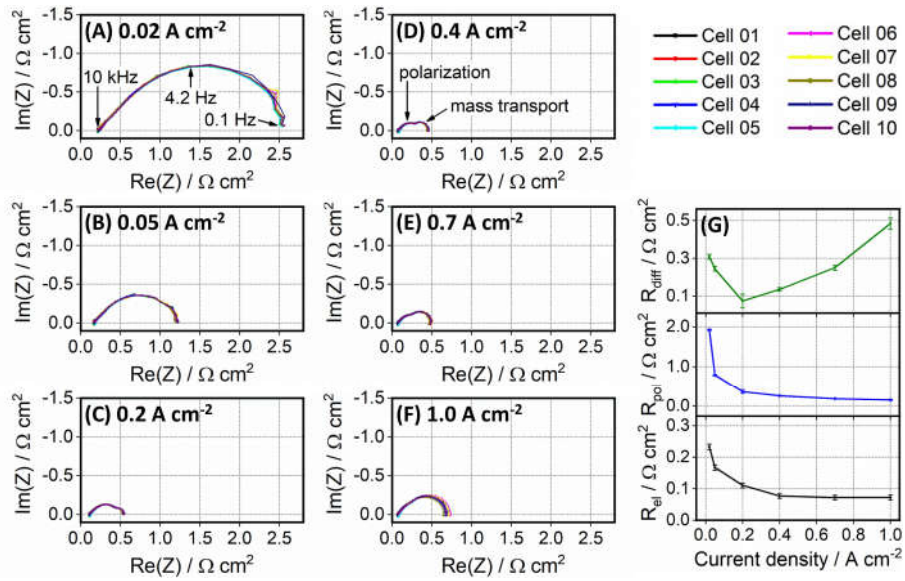


Figure 5: Nyquist plots of the impedance analysis of all individual cells under operating points as indicated in Figure 3 ((A) to (F)). Results of EIS fitting is provided in (G) using the equivalent circuit given in Figure 2 (A); presented values are average values of data from all single cells and included error bars represent standard deviation of single cell data.

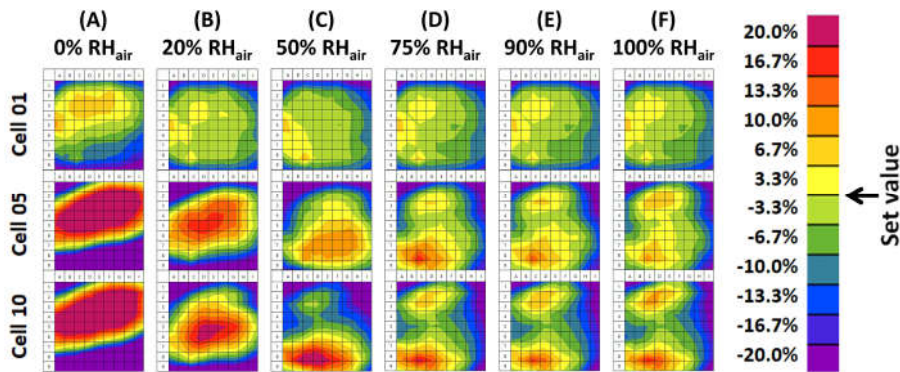


Figure 6: Impact of air inlet humidity (RH_{air}) on current density distribution at 0.5 A cm^{-2} . Results are shown for RH_{air} of 0% (A), 20% (B), 50% (C), 75% (D), 90% (E), and 100% (F). Results are presented in relative values and scaled to $\pm 20\%$ deviation from the set value of 0.5 A cm^{-2} . Cell and media flow configuration is given in Figure 1.

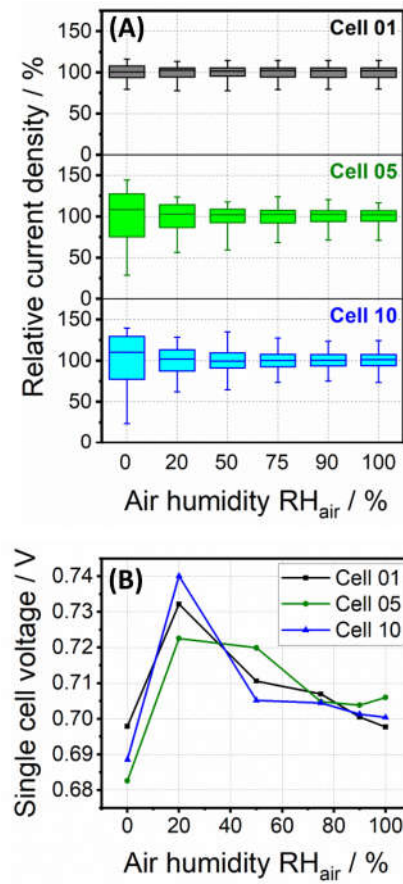


Figure 7: Box-Whisker plots (A) of the current density distribution measurements shown in Figure 6. Single cell voltages of the three analyzed cells at different operating points are shown in panel (B).

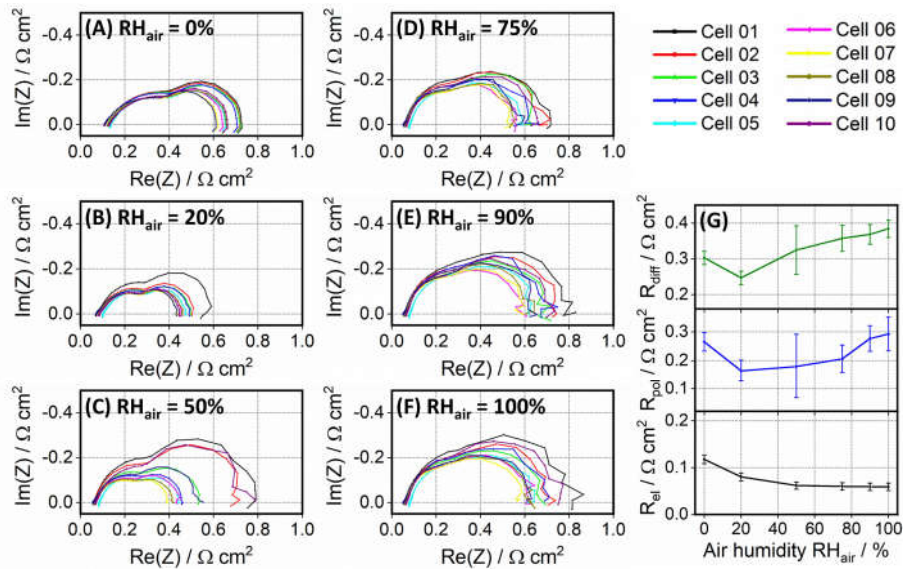


Figure 8: Impact of air inlet humidity (RH_{air}) on impedance response at 0.5 A cm^{-2} . Nyquist plots are shown for RH_{air} of 0% (A), 20% (B), 50% (C), 75% (D), 90% (E), and 100% (F). Results of EIS fitting is provided in (G) using the equivalent circuit given in Figure 2 (A); presented values are average values of data from all single cells and included error bars represent standard deviation of single cell data.

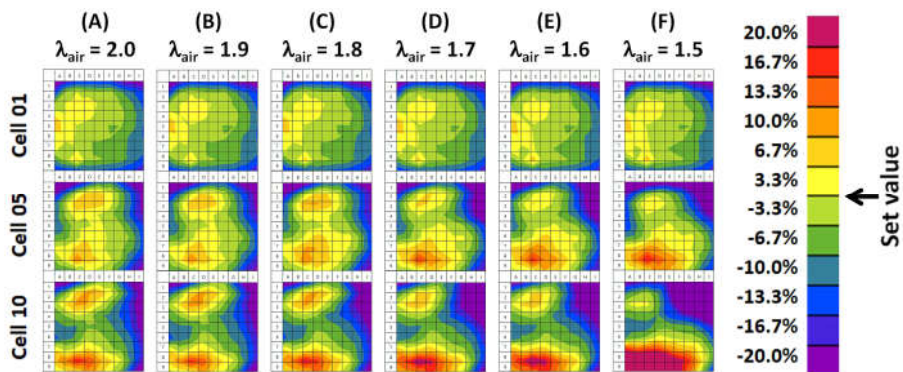


Figure 9: Impact of air stoichiometry (λ_{air}) on current density distribution at 0.5 A cm^{-2} . Results are shown for λ_{air} of 2.0 (A), 1.9 (B), 1.8 (C), 1.7 (D), 1.6 (E), and 1.5 (F). Results are presented in relative values and scaled to $\pm 20\%$ deviation from the set value of 0.5 A cm^{-2} . Cell and media flow configuration is given in Figure 1.

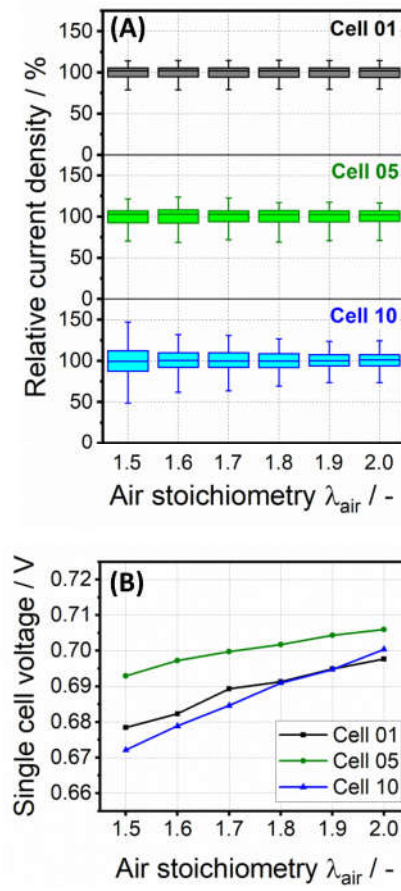


Figure 10: Box-Whisker plots (A) of the current density distribution measurements shown in Figure 9. Single cell voltages of the three analyzed cells at different operating points are shown in panel (B).

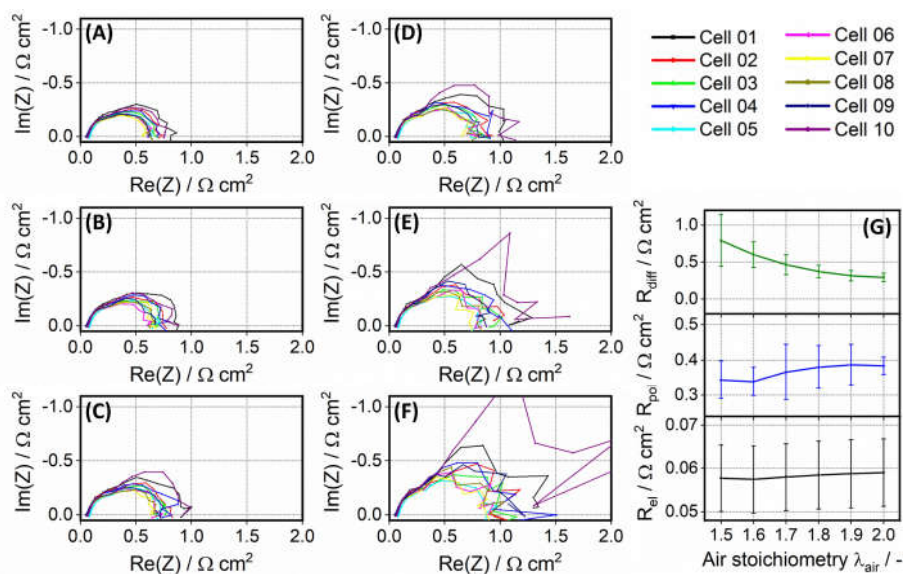


Figure 11: Impact of air stoichiometry (λ_{air}) on impedance response at 0.5 A cm^{-2} . Nyquist plots are shown for λ_{air} of 2.0 (A), 1.9 (B), 1.8 (C), 1.7 (D), 1.6 (E), and 1.5 (F). Results of EIS fitting is provided in (G) using the equivalent circuit given in Figure 2 (A); presented values are average values of data from all single cells and included error bars represent standard deviation of single cell data.

Tables

Table 1: DC and AC parameters for EIS data acquisition.

Current density / A cm ⁻²	DC load / A	AC amplitude / A
0.02	1.9	0.1
0.05	4.8	0.4
0.2	19.2	1.9
0.4	38.4	3.8
0.5	48.0	3.8
0.7	67.2	3.8
1.0	96.0	3.8